

Temperature- and frequency-dependent optical and transport conductivities in doped buckled honeycomb lattices

Andrii Iurov,^{1,*} Godfrey Gumbs,^{2,3} and Danhong Huang⁴

¹*Center for High Technology Materials, University of New Mexico, 1313 Goddess SE, Albuquerque, New Mexico 87106, USA*

²*Department of Physics and Astronomy, Hunter College of the City University of New York, 695 Park Avenue, New York, New York 10065, USA*

³*Donostia International Physics Center (DIPC), Paseo de Manuel Lardizabal 4, 20018 San Sebastian, Basque Country, Spain*

⁴*Air Force Research Laboratory, Space Vehicles Directorate, Kirtland Air Force Base, New Mexico 87117, USA*



(Received 9 April 2018; revised manuscript received 5 July 2018; published 13 August 2018)

Thermal and dynamical properties of optical and transport conductivities in doped buckled honeycomb lattices are studied for various doping densities and band gaps. At finite temperatures, a thermally convoluted polarization function is calculated by employing analytically derived temperature-dependent chemical potentials. With this finite-temperature polarization function, the optical conductivity, originating from an induced polarization current, is obtained in the long-wavelength limit, where both steps and negative peaks are shown as a function of frequency in its real and imaginary parts, respectively. Such spectral features can be used for analyzing plasmon dampings in silicene and ultrafast light modulations based on field-tunable band gaps. Additionally, in the presence of static screening, derived with the aid of the polarization function, for impurity elastic scattering, the transport conductivities are calculated for different doping densities and band gaps within the second-order Born approximation. The enhanced transport conductivity with a smaller band gap at intermediate temperatures will lead to high-mobility electron transistors for ultrafast electronics.

DOI: [10.1103/PhysRevB.98.075414](https://doi.org/10.1103/PhysRevB.98.075414)

I. INTRODUCTION

The successful mechanical exfoliation of group-IV and -V layered materials has spurred a substantial amount of interest in two-dimensional (2D) materials in condensed matter physics (see Ref. [1] and other references therein). Their planar or buckled structures, lattice asymmetry, nanoscale thickness, as well as their stacking configurations cause these 2D materials to possess some unusual physical and chemical properties. This causes some of them to have interesting electronic, optoelectronic, and spintronic device applications. Other buckled group-IV hexagonal 2D lattices include germanene [2–8] and others. Free-standing germanium allotropes had been previously predicted to be stable, low-buckled honeycomb structures with a much larger band gap (~ 23.9 meV) opened by spin-orbit coupling (SOC). The experimentally determined linear V-shaped density of states (DoS) provides strong verification for a gapped Dirac dispersion relation in germanene [9].

The Hamiltonians used to model these buckled-lattice systems need to take into account the effect of SOC and interlayer atomic interactions. While graphene and silicene are two representatives of these established 2D materials, sharing many similar electronic properties due to a hexagonal lattice [10–13], the unique silicon-based 2D Kane-Mele topological insulator [14], however, has a relatively large spin-orbit band gap (~ 1.55 eV) which could be nearly doubled under an external strain [15,16]. The band gap is associated with sublattice asymmetry and leads to a tunable energy band structure in the presence of an external electric field [14,15,17–24], enabling potential applications

to ultrafast light modulation with a high extinction ratio for ultrawideband digital communications. All these effects can be attributed directly to a finite out-of-plane buckling caused by a larger ionic radius of a silicon atom compared to carbon and by the sp^3 hybridization of electronic orbitals [17,21] at the same time. These interesting band-gap properties also offer tremendous advantages to controlling a current flow because electrons could be effectively confined by electrostatic gate voltages yielding variable potential barriers. More importantly, these silicene-based devices are compatible with silicon wafer processing in manufacturing silicon-based integrated circuits. Compelling experimental evidence for the existence of such graphene-like lattices while synthesizing epitaxial silicene sheets on silver is shown and discussed in Ref. [15].

There have been a number of key reports on silicene's thermal conductivity and transport coefficients [25–27], molecular dynamics studies [28], first-principle calculations of electron-phonon coupling and its effects on electron mobility [29], unusual thermoelectric behavior in Rashba spintronic materials [30], inhomogeneous quantum critical fluids [31], effects of anisotropy in phosphorenes [32], and detailed Monte Carlo studies [33].

The works in Refs. [34,35] presented detailed fundamental studies of ac and dc transport in buckled honeycomb lattices, including the calculations of spin and charge currents for individual valleys, investigation of the thermospin effect, and modification of the Kubo formalism by adding an effective magnetization to their model. It has been shown that the spin- and valley-Hall conductivities exhibit a strong temperature dependence. Another theoretical paper [36] on quantum spin- and valley-Hall effects was devoted to a spin-separation process by the valley-Hall effect in the absence of a magnetic field,

*Corresponding author: aiurov@unm.edu

which could be important for potential device applications. A study on optical response of silicene and other low-buckled structures under electron doping was reported in Ref. [37]; it demonstrated a strong dependence of its conductivity on a field-induced band gap.

In a pioneering work [38], analytic calculation for the conductivity of free-standing graphene in the frequency and wave vector domains was performed at various temperatures. It was demonstrated that, for each chosen temperature range, a simple analytical expression for the conductivity could be derived [39]. At low enough temperatures and carrier concentrations, the interband contribution is shown to play a leading role.

The semiclassical Boltzmann transport theory has been extensively used for hot electrons in semiconductor quantum-wire systems beyond the relaxation-time approximation [40–42]. Boltzmann transport in the presence of scattering by ionized impurities has been investigated thoroughly for graphene for a low bias field [43–45], demonstrating agreement between theory and available experimental data [46,47]. Carrier transport has also been studied in bilayer graphene [48] and in low-density silicon inversion layers [49].

However, the combined effects due to doping and finite temperatures on the electron transport in buckled honeycomb lattices with two diverse energy subbands and band gaps have not been explored extensively and will be chosen as the principal focus here.

The rest of our paper is organized as follows. We first briefly introduce the low-energy Hamiltonian and obtain associated electronic states in Sec. II for buckled honeycomb lattices. For doped silicene, we study the chemical potential at an arbitrary temperature using linear DoS for a wide class of gapped Dirac structures [50]. Applying the random-phase approximation (RPA), we further compute in Sec. III the dynamic polarization function and discuss its limiting behaviors at either small wave vectors or low frequencies, which become crucial in determining optical [51] and transport [52] conductivities, respectively. In Sec. IV, both the optical- and transport-conductivity calculations are performed, along with displayed numerical results, in the long-wavelength limit for incident light and within the screened second-order Born approximation for elastic scattering. For silicene, there exist two inequivalent subbands and both intra- and intersubband impurity scatterings are considered for energy-relaxation time of doped electrons. Finally, our concluding remarks providing an overview are provided in Sec. V.

II. LOW-ENERGY ELECTRONIC STATES AND CHEMICAL POTENTIAL

We begin this section by exploiting previously reported band-structure models for low-energy electronic states of buckled honeycomb lattices. We first consider silicene as an example, but keep in mind that similar properties—e.g., constant internal spin-orbit band gap (Δ_{SO}) and field (\mathcal{E}_\perp) dependent sublattice-asymmetry band gap $\Delta_z \sim \mathcal{E}_\perp$, as well as two inequivalent subbands—could also be applied to germanene.

The low-energy dispersion relations for a buckled honeycomb lattice, obtained from a block-diagonal Hamiltonian

matrix [17,24], have been shown to be

$$\varepsilon_{\xi,\sigma}^\gamma(k) = \gamma \sqrt{(\xi\sigma\Delta_z - \Delta_{SO})^2 + (\hbar v_F k)^2} \equiv \varepsilon_\beta^\gamma(k), \quad (1)$$

where $\mathbf{k} = (k_x, k_y)$ is a 2D wave vector of electrons, v_F the Fermi velocity, $\sigma = \pm 1$ a real spin index, and $\xi = \pm 1$ a valley index. From these dispersions we obtain two symmetrical subbands for electrons ($\gamma = +1$) and holes ($\gamma = -1$), respectively. Here, each subband in Eq. (1) is specified by its two gap parameters $\Delta_{(\cdot)} = |\Delta_{SO} \mp \Delta_z|$, depending only on the composite indexes $\beta = \xi\sigma$. This composite index β will be used throughout this paper.

It is evident that both band gaps $\Delta_\beta = \Delta_{(\cdot)}$ depend on \mathcal{E}_\perp through Δ_z . By increasing \mathcal{E}_\perp from zero, $\Delta_<$ is reduced, which corresponds to a topological-insulator state for $\Delta_z < \Delta_{SO}$. When $\Delta_z = \Delta_{SO}$, we find $\Delta_< = 0$ for the lower gap. This unique state is referred to as the valley-spin polarized metal (VSPM) [17,24]. If $\Delta_z > \Delta_{SO}$, we return to the standard band-insulator (BI) phase.

In performing numerical calculations, energies and frequencies will be given in units of an energy scale $E_0 = 5.22$ meV, which corresponds to a gapless-graphene electron doping density $n_0 = 1 \times 10^{11}$ cm $^{-2}$. Here, the wave number is in units of $k_0 = E_0/\hbar v_F$, and the Fermi energy $E_F = E_0$ will be always assumed unless it is stated in figure captions for cases with varied E_F .

The silicene band structure in Eq. (1) gives rise to the following piecewise linear density of states (DoS) [35,37,53]:

$$\rho_d(\varepsilon) = \frac{\varepsilon}{\pi (\hbar v_F)^2} \sum_{\gamma=\pm 1} \sum_{\beta=(\cdot)} \Theta(\varepsilon/\gamma - \Delta_\beta), \quad (2)$$

where $\Theta(x)$ is the Heaviside step function, accounting for unavailable electronic states within the lower gap, as illustrated schematically in Fig. 6(a). Equation (2) can be employed to determine E_F at zero temperature ($T = 0$) with a fixed carrier density n_c , leading to [50,54]

$$2\pi (\hbar v_F)^2 n_c = \begin{cases} E_F^2 - \Delta_<^2 & \text{for } E_F < \Delta_>, \\ 2E_F^2 - (\Delta_<^2 + \Delta_>^2) & \text{for } E_F > \Delta_>. \end{cases} \quad (3)$$

Here, the upper subband is occupied only for $n_c \geq 2\Delta_{SO}\Delta_z/\pi\hbar^2v_F^2$, which corresponds to the second line in Eq. (3).

Moreover, the T -dependent chemical potential μ_T , which equals to E_F at $T = 0$, can be decided from the conservation of carrier numbers in thermal-equilibrium states. The details about the derivation of μ_T can be found from Ref. [50], which yields [50,53,55]

$$\pi \left(\frac{\hbar v_F}{k_B T} \right)^2 n_c = \sum_{\beta=(\cdot)} \sum_{\gamma=\pm 1} \left[-\text{Li}_2 \left(-e^{\frac{\gamma\mu_T - \Delta_\beta}{k_B T}} \right) + \frac{\Delta_\beta}{k_B T} \ln \left(1 + e^{\frac{\gamma\mu_T - \Delta_\beta}{k_B T}} \right) \right] \gamma, \quad (4)$$

where $\text{Li}_2(x)$ is a polylogarithm function, and n_c is related to E_F by Eq. (3). From Eq. (4) we find that μ_T depends on both T and E_F , as shown in Fig. 1, and the dependence is controlled by energy gaps $\Delta_<$ and $\Delta_>$. Furthermore, we find significant

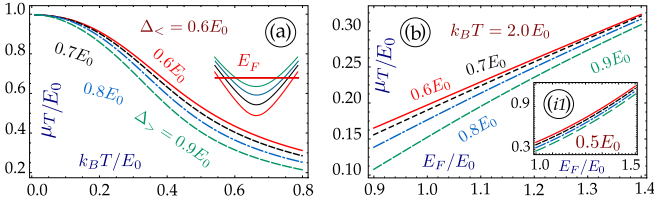


FIG. 1. Silicene μ_T dependence on T and E_F . Panel (a) shows μ_T as functions of $k_B T$ for $E_F/E_0 = 1$, $\Delta_</>/E_0 = 0.6$, and $\Delta_>/E_0 = 0.6$ (red solid curve), 0.7 (black short-dashed), 0.8 (blue dash-dotted), 0.9 (green dashed). Plot (b) displays μ_T as functions of E_F for $k_B T/E_0 = 2$ and $k_B T/E_0 = 0.5$ (inset). Here, colors and types of various curves for different Δ_β are defined in the same way as in (a).

difference in μ_T at low and intermediate T . For $k_B T \ll E_F$, Eq. (4) reduces to previous approximate results [56,57].

III. OPTICAL-POLARIZATION FUNCTION

We now turn our attention to an investigation of the dynamical polarization function $\Pi_T(q, \omega | \mu_T, \Delta_\beta)$ for n -doped silicene at arbitrary temperature. The function $\Pi_T(q, \omega | \mu_T, \Delta_\beta)$ is recognized as one of the most important quantities in characterizing optical properties of an electronic system. In order to account for screening effect on a Coulomb potential between two electrons, we use a dielectric function $\epsilon_T(q, \omega)$, which, under the random-phase approximation (RPA), takes the form

$$\epsilon_T(q, \omega) = 1 - v(q) \Pi_T(q, \omega | \mu_T, \Delta_\beta), \quad (5)$$

where $v(q) = 2\pi e^2/\epsilon_s q$ is the 2D Fourier-transformed Coulomb potential, and $\epsilon_s = 4\pi\epsilon_0\epsilon_b$ with ϵ_b as the background dielectric constant in which the 2D material is embedded. In Eq. (5), zeros of $\epsilon_T(q, \omega)$ determine the dispersion $\omega_{pl}(q)$ of plasmon excitations [58,59]. For silicene, these plasmon modes become spin and valley polarized and they also rely on an external electric field [60]. The full optical-polarization function is a sum [24] of two results for gapped graphene [59],

$$\Pi_T(q, \omega | \mu_T) = \sum_{\beta} \Pi_T(q, \omega | \mu_T, \Delta_\beta), \quad (6)$$

which depends on μ_T , $\Delta_</>$, and $\Delta_>$.

In the one-loop approximation, the dynamical polarization function in Eq. (6) at finite T is given by

$$\begin{aligned} \Pi_T(q, \omega | \mu_T, \Delta_\beta) &= \sum_{\gamma, \gamma'=\pm 1} \int \frac{d^2\mathbf{k}}{2\pi^2} \mathcal{F}_{\gamma, \gamma'}(\mathbf{k}, \mathbf{q} | \Delta_\beta) \\ &\times \frac{f_0(\epsilon_\beta^\gamma(k)) - f_0(\epsilon_\beta^{\gamma'}(|\mathbf{k} + \mathbf{q}|))}{\hbar\omega + i0^+ + \epsilon_\beta^\gamma(k) - \epsilon_\beta^{\gamma'}(|\mathbf{k} + \mathbf{q}|)}, \end{aligned} \quad (7)$$

where the electron transitions between different spins or valleys are excluded, $f_0(x) = \{1 + \exp[(x - \mu_T)/k_B T]\}^{-1}$ is the Fermi functions for thermal-equilibrium electrons and holes, and it reduces to Heaviside function $\Theta(E_F - \epsilon_\beta^\gamma(k))$ at $T = 0$. Meanwhile, the prefactor $\mathcal{F}_{\gamma, \gamma'}(\mathbf{k}, \mathbf{q} | \Delta_\beta)$ in Eq. (7) represents an overlap of the electron ($\gamma = +1$) and hole ($\gamma = -1$) wave

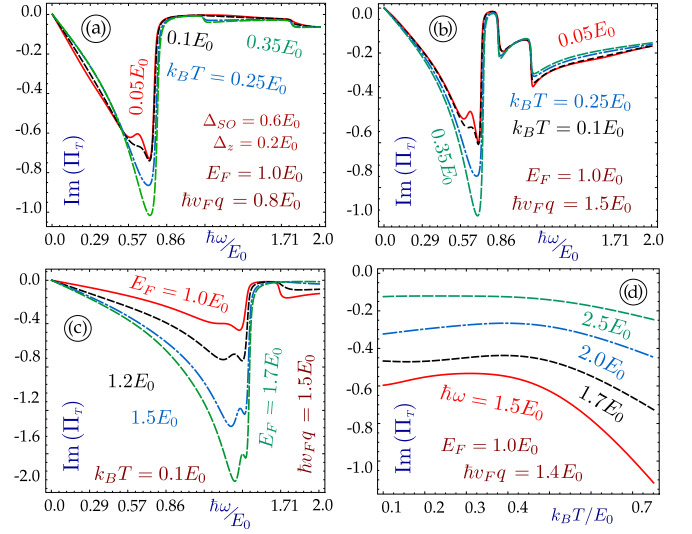


FIG. 2. $\text{Im}[\Pi_T(q, \omega | \mu_T, \Delta_\beta)]$ (in units of k_0^2/E_0) for silicene with $\Delta_{SO}/E_0 = 0.6$, $\Delta_z/E_0 = 0.2$ and various values of n_c . Panels (a)-(c) present $\hbar\omega$ dependence for $q = 0.8k_0$ (a), $1.5k_0$ (b) and (c). Different curves in (a) and (b) are associated with $E_F/E_0 = 1$, and $k_B T/E_0 = 0.05$ (red solid), 0.1 (black dashed), 0.25 (blue dash-dotted), 0.35 (green dashed). Panel (c) presents similar results for $k_B T/E_0 = 0.1$, and $E_F/E_0 = 1$ (red solid), 1.2 (black short-dashed), 1.5 (blue dash-dotted), 1.7 (green dashed). Plot (d) shows $k_B T$ dependence with $E_F/E_0 = 1$, $q = 1.4k_0$, and $\hbar\omega/E_0 = 1.5$ (red solid), 1.7 (black short-dash), 2 (blue dash-dotted), 2.5 (green dashed) for various curves.

functions of the same subband (fixed β for the same spin and valley) at two different wave vectors \mathbf{k} and $\mathbf{k} + \mathbf{q}$, i.e.,

$$2\mathcal{F}_{\gamma, \gamma'}(\mathbf{k}, \mathbf{q} | \Delta_\beta) = 1 + \gamma\gamma' \frac{(\hbar v_F)^2 \mathbf{k} \cdot (\mathbf{k} + \mathbf{q}) + \Delta_\beta^2}{|\epsilon_\beta^\gamma(k) \epsilon_\beta^{\gamma'}(|\mathbf{k} + \mathbf{q}|)|}. \quad (8)$$

Here, no valley or spin change under optical excitations is allowed so that only one index β occurs in Eq. (6), different from the summation over electron/hole indexes γ and γ' in Eq. (7) for pseudospins.

For ease of computation, instead of using Eq. (7) directly, we utilize a thermal-convolution technique [61] for $T > 0$ from the zero- T polarization function $\Pi^{(0)}(q, \omega | E_F, \Delta_\beta)$. Compared to Eq. (7), this approach has an advantage of dealing with a known analytic expression [24,58,59,62] for $\Pi^{(0)}(q, \omega | E_F, \Delta_\beta)$. This thermal convolution will be done for all accessible frequencies ω and wave numbers q , including the static and long-wavelength limits.

The imaginary part of $\Pi_T(q, \omega | \mu_T, \Delta_\beta)$ (associated with Landau damping) as functions of ω and T for various n_c (related to E_F) and T is presented in Fig. 2. The plasmon Landau damping has a resonance for fixed $q = 0.8k_0$ in (a), which becomes more significant with increasing T . In comparison with (a), a high-frequency shoulder-like feature develops as $q = 1.5k_0$ in (b). As doping density n_c (or E_F) is increased in (c) with $q = 1.5k_0$ and $k_B T/E_0 = 0.1$, the resonance in Landau damping is greatly enhanced and shifted to higher frequencies. However, for nonresonant Landau damping as a function of $k_B T$ in (d) with $E_F/E_0 = 1.0$ and $q = 1.4k_0$,

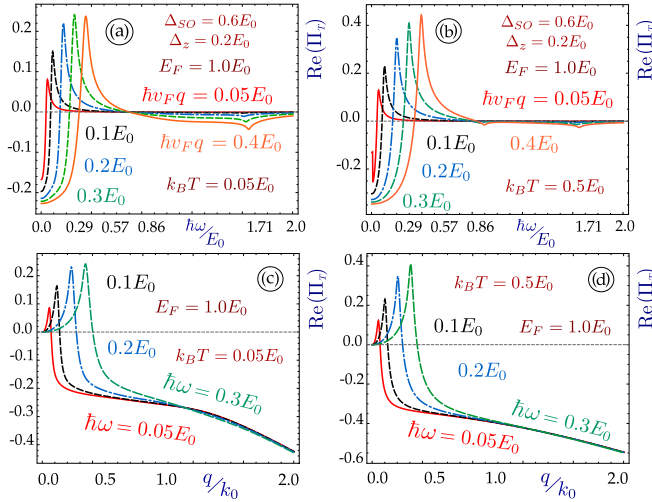


FIG. 3. $\text{Re}[\Pi_T(q, \omega | \mu_T, \Delta_\beta)]$ (in units of k_0^2/E_0) for silicene with $\Delta_{SO}/E_0 = 0.6$, $\Delta_z/E_0 = 0.2$, and $E_F/E_0 = 1$. Panels (a) and (b) show $\hbar\omega$ dependence for various curves with $q/k_0 = 0.05$ (red solid), 0.1 (black short-dashed), 0.2 (blue dash-dotted), 0.3 (green dashed), 0.4 (orange solid). Plots (c) and (d) demonstrate q dependence of curves with relatively small $\hbar\omega/E_0 = 0.05$ (red solid), 0.1 (black short-dashed), 0.2 (blue dash-dotted), 0.3 (green dashed). In addition, $k_B T/E_0 = 0.05$ in (a) and (c) while $k_B T/E_0 = 0.5$ in (b) and (d).

its reduction with T becomes less and less significant with increasing ω .

On the other hand, the real part of $\Pi_T(q, \omega | \mu_T, \Delta_\beta)$ as functions of ω and q for different fixed q and ω values are presented in Fig. 3. At $k_B T/E_0 = 0.05$, we find from (a) that the plasmon energy is pushed up by increase of q . This enhancement of plasmon energy with q (or the group velocity) becomes larger at a relatively high temperature $k_B T/E_0 = 0.5$ in (b). Similar increases of plasmon wave number can also be seen from (c) and (d) as the frequency ω goes up at both low and intermediate T , respectively.

IV. CONDUCTIVITIES

We now further proceed to conductivities for doped silicene by using the obtained T and E_F dependent optical-polarization function in Sec. III. We will mainly focus on optical conductivity, which is related to polarization function in the long-wavelength limit, as well as the transport conductivity, which is calculated based on semiclassical Boltzmann theory including the polarization function in the static limit.

A. Optical conductivity

The optical conductivity, which connects the polarization-current density (per atomic-layer thickness) to the incident electromagnetic field with various frequencies due to light-induced density fluctuations (mostly direct interband optical transitions of electrons), is often used in characterizing material optical properties, e.g., absorptions, transmissions, and reflections. For graphene, these optical properties were examined in both visible and infrared frequency ranges. In the

former case, graphene transmittance was predicted [63–65] to be independent of light frequency ω , and it was confirmed [66] by directly measuring the optical conductivity, reflectivity, and transmission for photon energies exceeding 200 meV. The calculations of graphene optical conductivity in the visible range using the next-nearest-neighbor tight-binding model justified the Dirac-cone approximations well above the normally accepted energy range. Applying the Dirac-cone approximation, we have shown [67] that the induced optical polarization in graphene affects the hybridization of radiative and evanescent electromagnetic fields, which results in localized polarization fields along with a modification of an incident surface plasmon-polariton field. Studies of Dirac quasiparticle transport in graphene under a magnetic field, e.g., Hall and optical conductivities, were reported in Ref. [68]. Additionally, a generalized model for the nonlinear optical conductivity of generic two-band systems (gapped or gapless graphene) demonstrated that such nonlinearities can be controlled by a single dimensionless parameter proportional to the incident-field strength [69].

The general relation between the optical conductivity and optical-polarization function was discussed by us before [51]. In the long-wavelength limit ($q \rightarrow 0$), an incident electromagnetic field can be treated as a spatially uniform one. In the following, we present a detailed study on the dependence of optical conductivity on T , E_F , and Δ_β in silicene. Under the long-wavelength limit, the optical conductivity for a weak incident light is simply related to the dynamical polarization function through [70,71]

$$\sigma_O^{(T)}(\omega | \mu_T, \Delta_\beta) = i\omega e^2 \lim_{q \rightarrow 0} \frac{\Pi_T(q, \omega | \mu_T, \Delta_\beta)}{q^2}. \quad (9)$$

Here, it is important to point out that $\Pi_T(q, \omega | \mu_T, \Delta_\beta) \sim q^2$ as $q \rightarrow 0$ for all 2D systems, regardless of the band gaps [59] and temperatures [54,57,72]. Therefore, the optical conductivity in Eq. (9) becomes independent of q . Meanwhile, such a limiting behavior in $\Pi_T(q, \omega | \mu_T, \Delta_\beta)$ also contributes a $\sim \sqrt{q}$ dependence to the plasmon dispersion relation.

By starting the case with $T = 0$, the polarization function for $q \rightarrow 0$ is given explicitly by [58,59,72]

$$\begin{aligned} & \text{Re}[\Pi^{(0)}(q, \omega | E_F, \Delta_\beta)] \\ &= \frac{q^2}{4\pi\hbar\omega} \sum_{\beta=\pm 1} \left\{ \frac{4E_F}{\hbar\omega} \left[1 - \left(\frac{\Delta_\beta}{E_F} \right)^2 \right] \right. \\ & \quad \left. + \left[1 + \left(\frac{2\Delta_\beta}{\hbar\omega} \right)^2 \right] \ln \left| \frac{2E_F - \hbar\omega}{2E_F + \hbar\omega} \right| \right\}, \\ & \text{Im}[\Pi^{(0)}(q, \omega | E_F, \Delta_\beta)] \\ &= -\frac{q^2}{4\hbar\omega} \Theta(\hbar\omega - 2E_F) \sum_{\beta=\pm 1} \left[1 + \left(\frac{2\Delta_\beta}{\hbar\omega} \right)^2 \right], \quad (10) \end{aligned}$$

where the logarithm term in $\text{Re}[\Pi^{(0)}(q, \omega | E_F, \Delta_\beta)]$ has a negligible contribution to the undamped plasmon dispersion relation for $\hbar\omega \ll E_F$ and it is often neglected in previous studies. Equation (10) leads to the so-called *absorption threshold* [63–65] defined as $\omega_0 \sim 2E_F/\hbar$

under which $\text{Im}[\Pi^{(0)}(q, \omega | E_F, \Delta_\beta)] = 0$, and it is independent of Δ_β . However, this logarithm term can still significantly affect $\text{Re}[\Pi^{(0)}(q, \omega | E_F, \Delta_\beta)]$ above this absorption threshold.

From Eq. (9) we know that the real (imaginary) part of $\sigma_O^{(T)}(\omega | \mu_T, \Delta_\beta)$ is related to the imaginary (real) part of $\Pi_T(q, \omega | \mu_T, \Delta_\beta)$. Using Eq. (10) we find for $T = 0$

$$\begin{aligned} & \text{Im}[\sigma_O^{(0)}(\omega | E_F, \Delta_\beta)] \\ &= \frac{e^2}{4\pi\hbar} \sum_{\beta=\pm 1} \left\{ \frac{4E_F}{\hbar\omega} \left[1 - \left(\frac{\Delta_\beta}{E_F} \right)^2 \right] \right. \\ & \quad \left. + \left[1 + \left(\frac{2\Delta_\beta}{\hbar\omega} \right)^2 \right] \ln \left| \frac{2E_F - \hbar\omega}{2E_F + \hbar\omega} \right| \right\}, \\ & \text{Re}[\sigma_O^{(0)}(\omega | E_F, \Delta_\beta)] \\ &= \frac{e^2}{4\hbar} \Theta(\hbar\omega - 2E_F) \sum_{\beta=\pm 1} \left[1 + \left(\frac{2\Delta_\beta}{\hbar\omega} \right)^2 \right], \end{aligned} \quad (11)$$

where $\text{Re}[\sigma_O^{(0)}(\omega | E_F, \Delta_\beta)] = 0$ as long as $\hbar\omega < 2E_F$, which is referred to as a *state-blocking effect* [66,68,69] due to Pauli exclusions and is attributed to the step-like distribution function at $T = 0$ in Eq. (7). At finite T , however, the step-like distribution function in Eq. (7) can still be approximated by [63,73]

$$\Theta(E_F - \varepsilon_\beta^\gamma(k)) \implies \frac{1}{2} \left\{ 1 - \tanh \left[\frac{\varepsilon_\beta^\gamma(k) - \mu_T}{2k_B T} \right] \right\}. \quad (12)$$

Consequently, the ω dependence in $\text{Re}[\sigma_O^{(T)}(\omega | \mu_T, \Delta_\beta)]$ will be smooth and nonzero. Furthermore, we know from Eqs. (10) and (12) that $\text{Im}[\Pi_T(q, \omega | \mu_T, \Delta_\beta)]$ is nonzero at finite T with a thermal tail. This leads to a nonzero $\text{Re}[\sigma_O^{(T)}(\omega | \mu_T, \Delta_\beta)]$ as a function of ω . We further expect that $\text{Re}[\sigma_O^{(T)}(\omega | \mu_T, \Delta_\beta)]$ will depend on T substantially since $\text{Im}[\Pi_T(q, \omega | \mu_T, \Delta_\beta)]$ decreases as $1/T$ in the high- T limit for all q values.

Making use of the results in Ref. [57], for gapless ($\Delta_\beta = 0$) but doped ($E_F > 0$) graphene we obtain a simple result for optical conductivity in the high- T limit ($k_B T \gg E_F$ and $\hbar\omega$):

$$\begin{aligned} & \sigma_O^{(T)}(\omega | \mu_T, \Delta_\beta = 0) \\ & \simeq \frac{e^2}{\hbar} \left\{ \frac{\hbar\omega}{16k_B T} \left[1 - \frac{1}{3} \left(\frac{\hbar\omega}{4k_B T} \right)^2 \right] \right. \\ & \quad \left. + i \frac{2 \ln 2 k_B T}{\pi \hbar\omega} \left[1 + 2 \ln 2 \left(\frac{E_F}{4 \ln 2 k_B T} \right)^4 \right] \right\}, \end{aligned} \quad (13)$$

where we have already employed the relation [57] $\mu_T \approx (E_F^2/4 \ln 2 k_B T)$ for high T . It is evident from Eq. (13) that $\text{Im}[\sigma_O^{(T)}(\omega | \mu_T, \Delta_\beta = 0)]$ is large but only weakly depends on E_F . Meanwhile, $\text{Re}[\sigma_O^{(T)}(\omega | \mu_T, \Delta_\beta = 0)]$ is small and decreases as $1/T$ within this high- T limit.

On the other hand, for gapped ($\Delta_\beta = \Delta_0$) but undoped ($E_F = 0$) graphene at high T ($k_B T \gg \Delta_0$ and $\hbar\omega$), we find

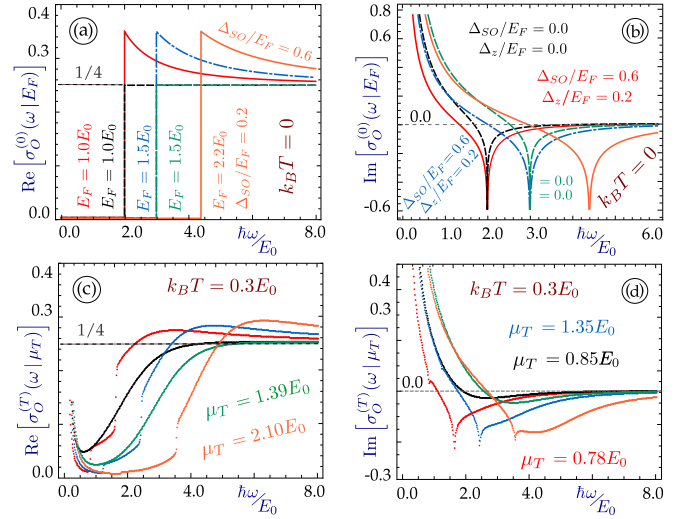


FIG. 4. $\sigma_O^{(T)}(\omega | \mu_T)$ (in units of e^2/\hbar) of silicene from Eq. (15) in the low- T regime. Panels (a), (c) show its real part as function of $\hbar\omega$, while panels (b), (d) give its imaginary part. Here, we take $T = 0$ for (a), (b) but $k_B T/E_0 = 0.3$ in (c), (d). Different curves correspond to $\Delta_{SO}/E_0 = 0.6$, $\Delta_z/E_0 = 0.2$, $E_F/E_0 = 1$ (red); $\Delta_{SO} = \Delta_z = 0$, $E_F/E_0 = 1$ (black); $\Delta_{SO}/E_0 = 0.9$, $\Delta_z/E_0 = 0.3$, $E_F/E_0 = 1.5$ (blue); $\Delta_{SO} = \Delta_z = 0$, $E_F/E_0 = 1.5$ (green); $\Delta_{SO}/E_0 = 1.32$, $\Delta_z/E_0 = 0.44$, $E_F/E_0 = 2.2$ (orange).

the optical conductivity

$$\begin{aligned} & \text{Re}[\sigma_O^{(T)}(\omega | \mu_T, \Delta_0)]_{E_F=0} = \frac{e^2}{16\hbar} \left(\frac{\hbar\omega}{k_B T} \right) \left(1 - \frac{\Delta_0}{\hbar\omega} \right), \\ & \text{Im}[\sigma_O^{(T)}(\omega | \mu_T, \Delta_0)]_{E_F=0} = \frac{4e^2}{\pi\hbar} \left(\frac{k_B T}{\hbar\omega} \right) \left\{ 2 \ln 2 - \left(\frac{\Delta_0}{k_B T} \right)^2 \right. \\ & \quad \left. \times \left[\mathbb{C}_0 - \ln \left(\frac{\Delta_0}{2k_B T} \right) \right] \right\}, \end{aligned} \quad (14)$$

where $\mathbb{C}_0 \simeq 0.79$ is a constant. It is interesting to note from Eq. (14) that the real and imaginary parts of $\sigma_O^{(T)}(\omega | \mu_T, \Delta_0)$ for $E_F = 0$ acquire an inverse dependence on $\hbar\omega/k_B T$. Again, $\text{Im}[\sigma_O^{(T)}(\omega | \mu_T, \Delta_0)]$ only weakly depends on Δ_0 . If T is really high, the thermal population of the upper Dirac cone cannot be ignored even for $E_F = 0$. In this case, the factor $k_B T/\hbar\omega$ in Eq. (14) plays a role similar to that of $E_F/\hbar\omega$ in Eq. (11) for the imaginary part of the optical conductivity at $T = 0$.

Finally, for silicene with two inequivalent band gaps $\Delta_\beta = \Delta_{>,<}$, the corresponding result is a summation over these two band gaps, yielding

$$\sigma_O^{(T)}(\omega | \mu_T) = \sum_{\beta=\pm 1} \sigma_O^{(T)}(\omega | \mu_T, \Delta_\beta). \quad (15)$$

Here, no analytical results for optical conductivity at intermediate T can be obtained. For this situation, we present our numerical results in Figs. 4 and 5.

The real and imaginary parts of $\Pi_T(q, \omega | \mu_T)$ are connected by the Kramers-Kronig relations, implying similar connections between the real and imaginary parts of $\sigma_O^{(T)}(\omega | \mu_T)$. Specifically, the discontinuities in $\text{Re}[\sigma_O^{(T)}(\omega | \mu_T)]$ can be related to the negative peaks in $\text{Im}[\sigma_O^{(T)}(\omega | \mu_T)]$, as shown

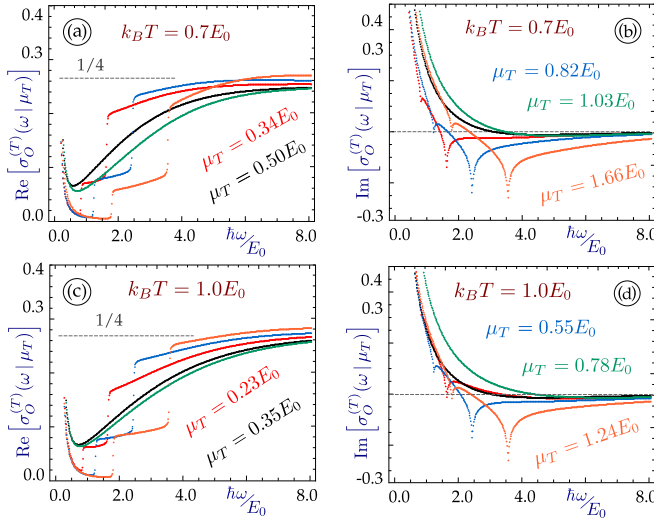


FIG. 5. $\sigma_O^{(T)}(\omega | \mu_T)$ (in units of e^2/\hbar) of silicene at intermediate T . Panels (a), (c) display its real part as function of $\hbar\omega$, while panels (b), (d) present its imaginary part. Here, we choose $k_B T/E_0 = 0.7$ for (a), (b) while $k_B T/E_0 = 1$ in (c), (d). Various curves are related to $\Delta_{SO}/E_0 = 0.6$, $\Delta_z/E_0 = 0.2$, $E_F/E_0 = 1$ (red); $\Delta_{SO} = \Delta_z = 0$, $E_F/E_0 = 1$ (black); $\Delta_{SO}/E_0 = 0.9$, $\Delta_z/E_0 = 0.3$, $E_F/E_0 = 1.5$ (blue); $\Delta_{SO} = \Delta_z = 0$, $E_F/E_0 = 1.5$ (green); $\Delta_{SO}/E_0 = 1.32$, $\Delta_z/E_0 = 0.44$, $E_F/E_0 = 2.2$ (orange).

in Figs. 4(a) and 4(b) for $T = 0$. Moreover, the peak positions depend on T , as seen from Figs. 4(b) and 4(d), mainly due to a nontrivial T dependence of μ_T (see the labels for calculated μ_T in Figs. 4 and 5). In fact, the steps or peaks at $T = 0$ are found exactly at the absorption threshold $\hbar\omega = 2E_F$. For high T , however, the absorption threshold for graphene is approximated by [63,65] $(\hbar\omega - 2E_F)^2 \Rightarrow (\hbar\omega - 2\mu_T)^2 + (2k_B T)^2$, where μ_T decreases with T . Consequently, the peak positions will not simply follow $\hbar\omega = 2\mu_T$ at finite T .

As seen from Fig. 4, the ω dependence in $\sigma_O^{(T)}(\omega | \mu_T)$ at low T is similar to the case of $T = 0$, where $\sigma_O^{(0)}(\omega | E_F)$ can be analytically calculated based on the derived expressions for $\Pi^{(0)}(q, \omega | E_F)$ in Ref. [24]. At $k_B T/E_0 = 0.3$, our systems with zero band gaps show no negative peaks in $\text{Im}[\sigma_O^{(T)}(\omega | \mu_T)]$, and $\text{Re}[\sigma_O^{(T)}(\omega | \mu_T)]$ only displays a smooth and monotonic increase (no discontinuities) with ω up to $1/4$. For intermediate T , as exhibited in Fig. 5, two steps (rising above $1/4$) and double peaks appear clearly in $\text{Re}[\sigma_O^{(T)}(\omega | \mu_T)]$ and $\text{Im}[\sigma_O^{(T)}(\omega | \mu_T)]$, respectively, due to the presence of two different continua for interband particle-hole modes (from different band gaps $\Delta_<$, $\Delta_>$). Even for $k_B T/E_0 = 1$, two negative peaks and jumps are still visible in Figs. 5(c) and 5(d).

B. Transport conductivity

We now turn to calculating the transport conductivity in doped silicene and gapped graphene in the presence of an elastic scattering of electrons by ionized impurities screened by a temperature-dependent dielectric function $\epsilon_T(q)$ determined from Eq. (5) under the static limit $\omega \rightarrow 0$. Based on the Boltzmann transport equation, effects of elastic, inelastic, and electron-pair scatterings were extensively studied by us

in semiconductors [40–42] and graphene [52] beyond the relaxation-time approximation [74] for a strong bias field. For a weak bias field, the Boltzmann theory was used in Ref. [56] for the transport conductivity of gapless graphene, showing a nonmonotonic temperature dependence. In the presence of band gaps, however, the nontrivial T dependence in μ_T must be taken into account, as discussed in Sec. II.

When the external bias voltage is very low in comparison with E_F , the general Boltzmann transport equation can be simplified by the relaxation-time approximation for particle collisions. Consequently, we obtain the transport conductivity for $\gamma = \gamma' = +1$ from

$$\sigma_B^{(T)}(\mu_T | \Delta_0) = \frac{e^2 v_F^2}{2} \int_{\Delta_0}^{\infty} d\varepsilon \left[-\frac{\partial f_0(\varepsilon)}{\partial \varepsilon} \right] \times \rho_d(\varepsilon) \tau_e^{(T)}(\varepsilon) \left(1 - \frac{\Delta_0^2}{\varepsilon^2} \right), \quad (16)$$

where $\rho_d(\varepsilon)$ is the DoS only for $\gamma = +1$, $\tau_e^{(T)}(\varepsilon)$ is the energy-relaxation time for driven carriers, and the factor $(1 - \Delta_0^2/\varepsilon^2)$ represents the reduction of group velocity by a band gap. For electron doping with $E_F > 0$ in gapped graphene, the integration in Eq. (16) is only carried out over the conduction band energies. At $T = 0$, we have $[-\partial f_0(\varepsilon)/\partial \varepsilon] \Rightarrow \delta(\varepsilon - E_F)$ and $E_F > \Delta_0$. For low temperatures $k_B T \ll E_F$, $[-\partial f_0(\varepsilon)/\partial \varepsilon]$ can still be approximated by $\delta(\varepsilon - E_F)$, and therefore only electrons around the Fermi energy E_F will contribute to conduction. For high temperatures $k_B T \gg E_F$, on the other hand, $[-\partial f_0(\varepsilon)/\partial \varepsilon]$ becomes nonzero for all energies outside the band gap region $\varepsilon > \Delta_0$. This situation is illustrated in Fig. 6(a) for silicene with two inequivalent band gaps $\Delta_\beta = \Delta_>$ or $\Delta_<$. Consequently, we expect that a large Δ_β value always reduces conductivities due to a smaller group velocity and a reduced DoS for contributions of low-energy electrons at high T , as seen from Fig. 6(b).

An important quantity in our conductivity calculation is the energy-relaxation time $\tau_e^{(T)}(\varepsilon | \Delta_\beta)$ calculated by the second-order Born approximation [56,75,76] for $\gamma = +1$ as

$$\frac{1}{\tau_e^{(T)}(\varepsilon | \Delta_\beta)} = \frac{2\pi N_i}{\hbar} \int \frac{d^2 \mathbf{k}'}{(2\pi)^2} \left| \frac{v(|\mathbf{k}' - \mathbf{k}|)}{\epsilon_T(|\mathbf{k}' - \mathbf{k}|)} \right|^2 \delta(\varepsilon_\beta^\gamma(k) - \varepsilon_\beta^\gamma(k')) \times \mathcal{F}_{\gamma, \gamma'}(\mathbf{k}, \mathbf{k}' | \Delta_\beta) (1 - \cos \theta_{\mathbf{k}, \mathbf{k}'}), \quad (17)$$

where N_i represents the impurity areal density, the intervalley impurity scattering is ignored due to very large momentum transfer, the energy-conservation constraint for elastic impurity scattering is employed, i.e., $\gamma = \gamma' = 1$, $\theta_{\mathbf{k}, \mathbf{k}'}$ is the elastic scattering angle [74], and $\epsilon_T(q) \equiv \epsilon_T(q, \omega = 0)$ given by Eq. (5). The overlap factor $\mathcal{F}_{\gamma, \gamma'}(\mathbf{k}, \mathbf{q} | \Delta_\beta)$ is determined from Eq. (21), and the angular dependence of the factor $\mathcal{F}_{1,1}(\mathbf{k}, \mathbf{q} | \Delta_0) (1 - \cos \theta)$ in Eq. (17) for $k = k_0$ and different values of Δ_0 is displayed in Fig. 6(c), from which we find that the results for two-dimensional electron gas (2DEG) and gapless monolayer graphene are quite different. The full backscattering ($\theta = \pi$) becomes very strong for 2DEG but vanishes for gapless graphene. A finite Δ_0 value lifts the full backscattering from zero in gapped graphene. The increase

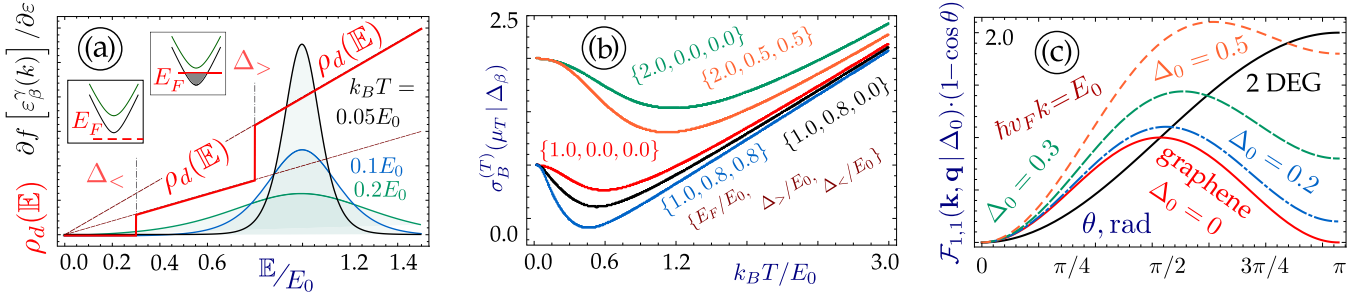


FIG. 6. Panel (a) shows the overlay of the two-step DoS $\rho_d(\mathbb{E})$ (in units of k_0^2/E_0) of silicene with $\partial f_0(\mathbb{E})/\partial \mathbb{E}$ (in units of E_0^{-1}) as functions of energy \mathbb{E} at various T . Plot (b) presents the transport conductivity $\sigma_B^{(T)}(\mu_T|\Delta_\beta)$ (in units of e^2/\hbar) as functions of $k_B T$ for different combinations of E_F/E_0 , $\Delta_</E_0$, and $\Delta_>/E_0$. Plot (c) displays the dimensionless factor $\mathcal{F}_{1,1}(\mathbf{k}, \mathbf{q}|\Delta_0)(1 - \cos \theta)$ as functions of scattering angle θ with fixed $k = k_0$ and different values of Δ_0 , where $|\mathbf{q}| = 2k \sin(\theta/2)$ and the result for 2DEG is also shown for a comparison.

of Δ_0 enhances the peak strength, pushes the peak θ value towards a larger one, and gradually enhances the scattering rate in Eq. (17). As a result, the energy-relaxation time $\tau_e^{(T)}(\varepsilon)$ in Eq. (16) decreases with Δ_0 , which provides an additional mechanism for a decreasing transport conductivity besides the reduced group velocity and DoS.

If graphene is subjected to an irradiation of circularly polarized light [77], the opened energy gap is found also leading to a monotonic decrease of the transport conductivity [78] by the ratio $\simeq (E_F^2 - \Delta_0^2)/(E_F^2 + 3\Delta_0^2)$, which is attributed to the decrease of the Fermi velocity from v_F for gapless graphene to $v_F[1 - (\Delta_0/E_F)^2]^{1/2}$ in the presence of a band gap Δ_0 .

Equation (17) could be further simplified due to the presence of the delta function for energy conservation in elastic scattering. Let us first consider gapped graphene with fourfold-degenerate energy subbands and a single, finite gap Δ_0 . One way is to perform the radial integration first with respect to \mathbf{k}' by using the delta function, which leads to

$$\frac{1}{\tau_e^{(T)}(\varepsilon|\Delta_0)} = \frac{2N_i}{\pi\hbar} \frac{\sqrt{\varepsilon_k^2 - \Delta_0^2}}{(\hbar v_F)^2} \int_0^1 d\xi \frac{\xi^2}{\sqrt{1-\xi^2}} \times \left\{ 1 + \frac{\Delta_0^2 + (1-2\xi^2)(\varepsilon_k^2 - \Delta_0^2)}{\varepsilon_k^2} \right\} \times \left(\frac{k\xi}{\alpha\pi} - \Pi_T(2\xi k, \omega = 0|\mu_T, \Delta_0) \right)^{-2}, \quad (18)$$

where $\varepsilon \equiv \varepsilon_k = \sqrt{(\hbar v_F k)^2 + \Delta_0^2} \geq \Delta_0$, and the expression in Eq. (21) for $\mathcal{F}_{1,1}(\mathbf{k}, \mathbf{k}' - \mathbf{k}|\Delta_0)$ has been employed. Alternatively, we can also calculate first the angular θ integration with respect to \mathbf{k}' under the condition $|\mathbf{k}| = |\mathbf{k}'|$, yielding

$$\frac{1}{\tau_e^{(T)}(\varepsilon|\Delta_0)} = \frac{N_i}{\pi\hbar} \frac{\varepsilon}{(\hbar v_F)^2} \int_0^{2k} \frac{dq}{k} \left(\frac{q}{k} \right)^2 \left[1 - \left(\frac{q}{2k} \right)^2 \right]^{-1/2} \times \left[1 + \frac{\Delta_0^2 + (\hbar v_F k)^2 (1 - 2q^2/k^2)}{\Delta_0^2 + (\hbar v_F k)^2} \right] \times \left[\frac{q}{2\pi\alpha} - \Pi_T(q, \omega = 0|\mu_T, \Delta_0) \right]^{-2}, \quad (19)$$

where $q = 2k \sin(\theta/2)$ and $k = \sqrt{\varepsilon^2 - \Delta_0^2}/(\hbar v_F)$.

Silicene has two inequivalent band gaps $\Delta_{(\cdot)}$, and we need to calculate the wave-function overlaps between these two different band gaps as a generalization of the result in Eq. (8). For this case, the pseudospin wave function is written as

$$\Psi_\beta^\gamma(\mathbf{k}|\Delta_\beta) = \frac{1}{\sqrt{2\mathbb{E}_\beta(k)}} \begin{bmatrix} \sqrt{\mathbb{E}_\beta(k) + \gamma\Delta_\beta} \\ \gamma\sqrt{\mathbb{E}_\beta(k) - \gamma\Delta_\beta} e^{i\Phi_\mathbf{k}} \end{bmatrix}, \quad (20)$$

where $\Phi_\mathbf{k} = \tan^{-1}(k_y/k_x)$ and $\mathbb{E}_\beta(k) = \varepsilon_\beta^\gamma(k)/\gamma = \sqrt{(\hbar v_F k)^2 + \Delta_\beta^2} = |\varepsilon_\beta^\gamma(k)|$. Therefore, it is straightforward to calculate the overlap from

$$\mathcal{F}_{\gamma,\gamma'}(\mathbf{k}, \mathbf{q}|\Delta_{1,2}) = \left| \langle \Psi_1^\gamma(\mathbf{k}|\Delta_1) | \Psi_2^{\gamma'}(\mathbf{k} + \mathbf{q}|\Delta_2) \rangle \right|^2 = \frac{1}{2} \left\{ 1 + \gamma\gamma' \frac{\Delta_1\Delta_2 + (\hbar v_F)^2 k|\mathbf{k} + \mathbf{q}| \cos \theta_{\mathbf{k}, \mathbf{k} + \mathbf{q}}}{\mathbb{E}_1(k)\mathbb{E}_2(|\mathbf{k} + \mathbf{q}|)} \right\}, \quad (21)$$

which reduces to Eq. (8) after taking $\Delta_1 = \Delta_2$ and $\mathbb{E}_1 = \mathbb{E}_2$. Here, we can apply a geometrical relation, i.e., $|\mathbf{k} + \mathbf{q}| \cos \theta_{\mathbf{k}, \mathbf{k} + \mathbf{q}} = k + q \cos \phi$ (see Fig. 7), so as to express the final result of Eq. (17) by an integration variable $\xi = -\cos \phi$, yielding

$$\frac{1}{\tau_e^{(T)}(\varepsilon|\Delta_\beta)} = \frac{1}{4} \sum_{i,j=1,2} \frac{1}{\tau_e^{(T)}(\varepsilon|\Delta_{i,j})}, \quad (22)$$

which includes electron transitions between a pair of states with either the same or different band gaps: $\mathbb{E}_i \implies \mathbb{E}_i$, $\mathbb{E}_i \implies \mathbb{E}_j$, $\mathbb{E}_j \implies \mathbb{E}_i$, and $\mathbb{E}_j \implies \mathbb{E}_j$. For a gapped graphene, we have $\Delta_1 = \Delta_2 = \Delta_0$ for all four terms in Eq. (22) and arrive at Eq. (18).

For two nondegenerate subbands in general, the allowed angle ϕ is determined by the following equation for the silicene lattice:

$$\cos \phi = \frac{\Delta_i^2 - \Delta_j^2}{2(\hbar v_F)^2 k q} - \frac{q}{2k}, \quad (23)$$

where each $\Delta_{i,j}$ could take either $\Delta_>$ or $\Delta_<$, i.e., three different ϕ values are possible for given k and q . If two band gaps become the same, there exists only one value from $\cos \phi = -q/2k$, as shown in Fig. 7.

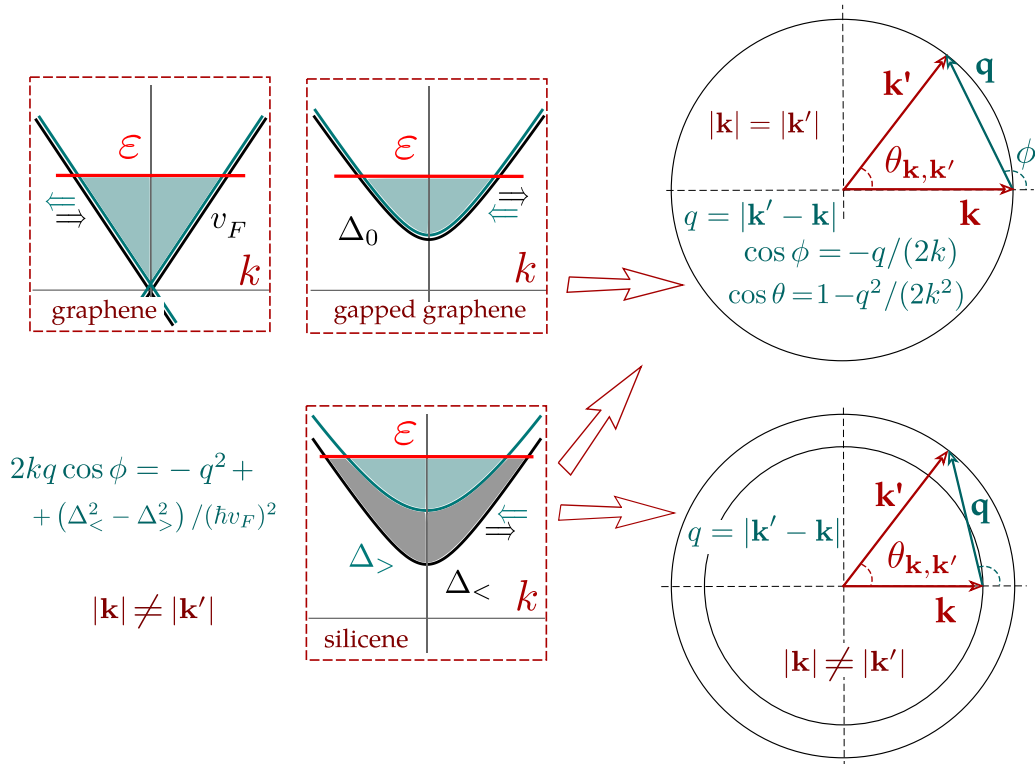


FIG. 7. Schematics for wave-vector relationships in an elastic scattering between $\varepsilon_{\beta=\pm 1}^{\nu=1}(k)$ and $\varepsilon_{\beta=\pm 1}^{\nu=1}(k')$ electron states with fourfold degeneracies $g_c = g_s, g_v = 4$ in graphene and partially degenerate subbands in silicene lattice. For the latter, intersubband transitions with different magnitudes of wave vectors ($|k| \neq |k'|$) are allowed.

For silicene at $T = 0$, the polarization function with two different band gaps $\Delta_\beta = \Delta_{(\cdot)} = |\Delta_{SO} + \beta\Delta_z|$ is given by [24,59]

$$\Pi^{(0)}(q, \omega = 0 | E_F, \Delta_\beta) = -\frac{E_F}{\pi} \sum_{\beta=\pm 1} f_{<}(q) \Theta(\Delta_\beta - E_F) + f_{>}(q) \Theta(E_F - \Delta_\beta), \quad (24)$$

where

$$f_{<}(q) = \frac{\Delta_\beta}{2E_F} + \left(\frac{\hbar v_F q}{4E_F} - \frac{\Delta_\beta^2}{4\hbar v_F q E_F} \right) \times \arcsin \left(\sqrt{1 + \left(\frac{2\Delta_\beta}{\hbar v_F q} \right)^2} \right),$$

$$f_{>}(q) = 1 - \Theta(q - 2k_F^\beta) \left[\frac{1}{2} \sqrt{1 - \left(\frac{2k_F^\beta}{q} \right)^2} - \left(\frac{\hbar v_F q}{4E_F} - \frac{\Delta_\beta^2}{4\hbar v_F q E_F} \right) \times \arctan \left(\frac{\hbar v_F \sqrt{q^2 - 4(k_F^\beta)^2}}{2E_F} \right) \right]. \quad (25)$$

Here, two inequivalent Fermi wave numbers $k_F^\beta = \sqrt{E_F^2 - \Delta_\beta^2}/\hbar v_F$ depend on band gaps Δ_β . For gapped graphene, this result is simplified by the substitution $\Delta_{(\cdot)} = \Delta_0$.

Our numerical results for the energy-relaxation rate $1/\tau_e^{(T)}(\varepsilon | \Delta_\beta)$ and the transport conductivity $\sigma_B^{(T)}(\mu_T | \Delta_\beta)$ are presented in Fig. 8. $\sigma_B^{(T)}(\mu_T | \Delta_\beta)$ in Fig. 8(c) is found to increase with T due to thermal occupations of high-energy states in the upper subband with a larger group velocity. On the other hand, as T increases, the enhanced screening to the impurity scattering will reduce the energy-relaxation rate, as exhibited in Figs. 8(a) and 8(b). Moreover, the polarization function is expected to decrease with a band gap at all temperatures, especially showing a $[1 - (\Delta_0/E_F)^2]$ dependence at $T = 0$ in the long-wavelength limit.

V. CONCLUDING REMARKS

We have carried out calculations to investigate the optical and transport properties, i.e., the polarizability and transport current conductivity, for doped buckled honeycomb lattices with two inequivalent energy subbands. Emphasis has been placed on the effects of finite dopings and temperatures on the conductivities, i.e., by considering doped systems at arbitrary temperatures.

In our calculations, the dynamical polarization function is found to play a key role in studies of both optical and transport

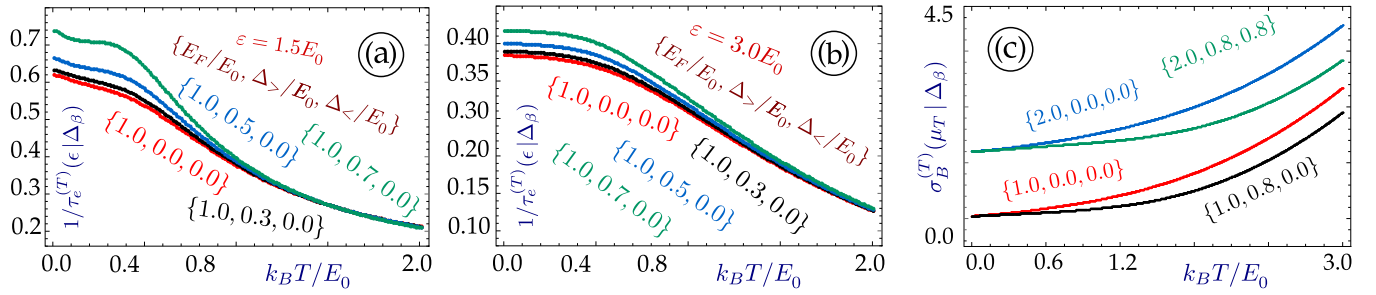


FIG. 8. $1/\tau_e^{(T)}(\epsilon|\Delta_\beta)$ (in units of E_0/\hbar) and $\sigma_B^{(T)}(\mu_T|\Delta_\beta)$ (in units of e^2/h) for silicene at various T . Plots (a) and (b) present the T dependence of $1/\tau_e^{(T)}(\epsilon|\Delta_\beta)$ for $E_F/E_0 = 1.0$, $\Delta_> = \Delta_< = 0$ (red), $E_F/E_0 = 1.0$, $\Delta_>/E_0 = 0.3$, $\Delta_< = 0$ (black), $E_F/E_0 = 1.0$, $\Delta_>/E_0 = 0.5$, $\Delta_< = 0$ (blue), and $E_F/E_0 = 1.0$, $\Delta_>/E_0 = 0.7$, $\Delta_< = 0$ (green). Panel (a) corresponds to $\epsilon/E_0 = 1.5$, while plot (b) corresponds to $\epsilon/E_0 = 3.0$. Panel (c) shows the T dependence of $\sigma_B^{(T)}(\mu_T|\Delta_\beta)$ for silicene with $E_F/E_0 = 1.0$, $\Delta_> = \Delta_< = 0$ (red), $E_F/E_0 = 1.0$, $\Delta_>/E_0 = 0.8$, $\Delta_< = 0$ (black), $E_F/E_0 = 2.0$, $\Delta_> = \Delta_< = 0.8$ (blue), and $E_F/E_0 = 2.0$, $\Delta_> = \Delta_< = 0$ (green).

currents. For finite temperatures, the polarizability is computed either through a thermal-convolution approach starting with a zero-temperature one, or by a direct substitution of the Fermi functions. In either case, it is necessary to find out in advance a temperature-dependent chemical potential or a thermal path for a chosen system. Quite different from the two-dimensional electron gases, the calculated chemical potential decreases with temperature but never reaches zero for band structures with an electron/hole symmetry, such as silicene. In fact, the chemical potential increases monotonically with doping density (or Fermi energy) at all temperatures but becomes more significant at low densities or high temperatures. The unique temperature dependence found in a chemical potential due to thermal populations of an upper subband leads to specific thermal features in both the dynamical polarization function and static screening to electron-impurity interactions included in the Boltzmann transport equation. The interplay between electron doping and temperature in the real and imaginary parts of a dynamical polarization function is found to be nontrivial due to the existence of dual band gaps. All of these physical effects have been applied to the Boltzmann transport equation.

Starting with some known results for the polarizability in gapless graphene, we have derived analytic expressions for the optical conductivities for gapped graphene and silicene in both zero-temperature and high-temperature limits. At zero temperature, the existing negative peaks in $\text{Im}[\sigma_O^{(T)}(\omega|\mu_T)]$ correspond to the absorption threshold at $\hbar\omega = 2E_F$, independent of band gaps. Instead, the band gaps do affect the nonrectangular shape of steps in $\text{Re}[\sigma_O^{(T)}(\omega|\mu_T)]$. At finite temperatures, the sharp step is rounded off and the negative peaks shift to low frequencies. Physically, both steps and negative peaks originate from the intraband particle-hole modes in the $q \rightarrow 0$ limit, which depend on temperature but not through the chemical potential. Each peak has been calculated and identified. The thermal shift of a negative peak ($\hbar\omega = 2E_F$ at $T = 0$) in the imaginary part of an optical conductivity does not follow the expected $\hbar\omega = 2\mu_T(E_F, T)$ temperature dependence and has been attributed to thermal variations in the boundaries of two separated continua with respect to different intersubband particle-hole

modes under dual band gaps. These unique spectra features can be applied to study plasmon damping in silicene and used for ultrafast light modulators based on field-tuned band gaps.

Finally, we have also explored the transport conductivity $\sigma_B^{(T)}(\mu_T|\Delta_\beta)$ within the energy-relaxation-time approximation for gapped graphene and silicene. By extending the semianalytic expressions for gapless-graphene inverse-relaxation time obtained in Ref. [56] to finite band gaps, we have found a significant reduction in $\sigma_B^{(T)}(\mu_T|\Delta_\beta)$ at low temperatures. In the presence of two inequivalent subbands of silicene, we have observed that $\sigma_B^{(T)}(\mu_T|\Delta_\beta)$ increases with temperatures and doping densities due to enhanced group velocities at higher electron energies as well as due to enlarged screening to the impurity scattering at the same time. Contrary to previously considered graphene with or without energy band gap, the inclusion of two new band gaps in buckled honeycomb lattices gives rise to additional intersubband elastic-scattering channels. As a result, more electron transitions can contribute to an energy-relaxation rate, which dramatically modifies the electron dynamics in Boltzmann transport.

In comparison with the Kubo formula for band transports, the use of the Boltzmann transport equation for doped buckled honeycomb lattices at finite temperatures has its own advantages in rigorously treating particle collisions. For elastic scattering of electrons with impurities, we have calculated explicitly the energy-dependent relaxation rate within the second-order Born approximation, instead of treating it as a phenomenological parameter as in Kubo's formula. These findings for transport conductivities are useful for investigating electron dynamics in innovative gapped Dirac materials and can be applied to quantum-ballistic bipolar electronic devices.

ACKNOWLEDGMENT

D.H. would like to acknowledge financial support from the Laboratory University Collaboration Initiative (LUCI) program and from the Air Force Office of Scientific Research (AFOSR).

- [1] A. Kara, H. Enriquez, A. P. Seitsonen, L. C. Lew Yan Voon, S. Vizzini, B. Aufray, and H. Oughaddou, *Surf. Sci. Rep.* **67**, 1 (2012).
- [2] Z. Ni, Q. Liu, K. Tang, J. Zheng, J. Zhou, R. Qin, Z. Gao, D. Yu, and J. Lu, *Nano Lett.* **12**, 113 (2011).
- [3] M. Dávila, L. Xian, S. Cahangirov, A. Rubio, and G. Le Lay, *New J. Phys.* **16**, 095002 (2014).
- [4] L. Li, S.-Z. Lu, J. Pan, Z. Qin, Y.-Q. Wang, Y. Wang, G.-Y. Cao, S. Du, and H.-J. Gao, *Adv. Mater.* **26**, 4820 (2014).
- [5] A. Acun, L. Zhang, P. Bampoulis, M. Farmanbar, A. van Houselt, A. Rudenko, M. Lingenfelder, G. Brocks, B. Poelsema, M. Katsnelson *et al.*, *J. Phys.: Condens. Matter* **27**, 443002 (2015).
- [6] L. Zhang, P. Bampoulis, A. van Houselt, and H. J. Zandvliet, *Appl. Phys. Lett.* **107**, 111605 (2015).
- [7] P. Bampoulis, L. Zhang, A. Safaei, R. Van Gastel, B. Poelsema, and H. J. W. Zandvliet, *J. Phys.: Condens. Matter* **26**, 442001 (2014).
- [8] M. Derivaz, D. Dentel, R. Stephan, M.-C. Hanf, A. Mehdaoui, P. Sonnet, and C. Pirri, *Nano Lett.* **15**, 2510 (2015).
- [9] C. Walhout, A. Acun, L. Zhang, M. Ezawa, and H. Zandvliet, *J. Phys.: Condens. Matter* **28**, 284006 (2016).
- [10] A. K. Geim and K. S. Novoselov, *Nat. Mater.* **6**, 183 (2007).
- [11] K. S. Novoselov, A. K. Geim, S. Morozov, D. Jiang, M. Katsnelson, I. Grigorieva, S. Dubonos, and A. A. Firsov, *Nature (London)* **438**, 197 (2005).
- [12] Y. Zhang, Y.-W. Tan, H. L. Stormer, and P. Kim, *Nature (London)* **438**, 201 (2005).
- [13] C. R. Dean, A. F. Young, I. Meric, C. Lee, L. Wang, S. Sorgenfrei, K. Watanabe, T. Taniguchi, P. Kim, K. L. Shepard *et al.*, *Nat. Nanotechnol.* **5**, 722 (2010).
- [14] C.-C. Liu, W. Feng, and Y. Yao, *Phys. Rev. Lett.* **107**, 076802 (2011).
- [15] P. Vogt, P. De Padova, C. Quaresima, J. Avila, E. Frantzeskakis, M. C. Asensio, A. Resta, B. Ealet, and G. Le Lay, *Phys. Rev. Lett.* **108**, 155501 (2012).
- [16] H. Xie, T. Ouyang, É. Germaneau, G. Qin, M. Hu, and H. Bao, *Phys. Rev. B* **93**, 075404 (2016).
- [17] M. Ezawa, *New J. Phys.* **14**, 033003 (2012).
- [18] B. Aufray, A. Kara, S. Vizzini, H. Oughaddou, C. Leandri, B. Ealet, and G. Le Lay, *Appl. Phys. Lett.* **96**, 183102 (2010).
- [19] P. De Padova, C. Quaresima, C. Ottaviani, P. M. Sheverdyeva, P. Moras, C. Carbone, D. Topwal, B. Olivieri, A. Kara, H. Oughaddou *et al.*, *Appl. Phys. Lett.* **96**, 261905 (2010).
- [20] B. Lalmi, H. Oughaddou, H. Enriquez, A. Kara, S. Vizzini, B. Ealet, and B. Aufray, *Appl. Phys. Lett.* **97**, 223109 (2010).
- [21] M. Ezawa, *Phys. Rev. Lett.* **109**, 055502 (2012).
- [22] C. J. Tabert and E. J. Nicol, *Phys. Rev. B* **87**, 235426 (2013).
- [23] C. J. Tabert and E. J. Nicol, *Phys. Rev. B* **88**, 085434 (2013).
- [24] C. J. Tabert and E. J. Nicol, *Phys. Rev. B* **89**, 195410 (2014).
- [25] X. Wang, Y. Hong, P. K. Chan, and J. Zhang, *Nanotechnology* **28**, 255403 (2017).
- [26] A. Feyzi and R. Chegel, *Eur. Phys. J. B* **89**, 193 (2016).
- [27] N. Ma and D. Jena, *Phys. Rev. X* **4**, 011043 (2014).
- [28] M. Kamatagi and N. Sankeshwar, in *Solid State Physics: Proceedings of the 59th DAE Solid State Physics Symposium 2014*, edited by D. Bhattacharyya, R. Chitra, and N. K. Sahoo, AIP Conf. Proc. No. 1665 (AIP, New York, 2015), p. 110036.
- [29] T. Gunst, T. Markussen, K. Stokbro, and M. Brandbyge, *Phys. Rev. B* **93**, 035414 (2016).
- [30] C. Xiao, D. Li, and Z. Ma, *Phys. Rev. B* **93**, 075150 (2016).
- [31] A. Lucas, J. Crossno, K. C. Fong, P. Kim, and S. Sachdev, *Phys. Rev. B* **93**, 075426 (2016).
- [32] Y. Liu and P. P. Ruden, *Phys. Rev. B* **95**, 165446 (2017).
- [33] P. Borowik, J.-L. Thobel, and L. Adamowicz, *Semicond. Sci. Technol.* **31**, 115004 (2016).
- [34] V. Vargiamidis, P. Vasilopoulos, and G. Q. Hai, *J. Phys.: Condens. Matter* **26**, 345303 (2014).
- [35] V. P. Gusynin, S. G. Sharapov, and A. A. Varlamov, *Phys. Rev. B* **90**, 155107 (2014).
- [36] M. Tahir, A. Manchon, K. Sabeeh, and U. Schwingenschlögl, *Appl. Phys. Lett.* **102**, 162412 (2013).
- [37] L. Stille, C. J. Tabert, and E. J. Nicol, *Phys. Rev. B* **86**, 195405 (2012).
- [38] L. Falkovsky and A. Varlamov, *Eur. Phys. J. B* **56**, 281 (2007).
- [39] L. Falkovsky, *J. Exp. Theor. Phys.* **106**, 575 (2008).
- [40] S. K. Lyo and D. H. Huang, *Phys. Rev. B* **64**, 115320 (2001).
- [41] S. K. Lyo and D. H. Huang, *Phys. Rev. B* **68**, 115317 (2003).
- [42] S. K. Lyo and D. H. Huang, *Phys. Rev. B* **73**, 205336 (2006).
- [43] E. H. Hwang, S. Adam, and S. Das Sarma, *Phys. Rev. Lett.* **98**, 186806 (2007).
- [44] S. Adam, E. Hwang, and S. D. Sarma, *Phys. E* **40**, 1022 (2008).
- [45] S. D. Sarma, S. Adam, E. Hwang, and E. Rossi, *Rev. Mod. Phys.* **83**, 407 (2011).
- [46] K. I. Bolotin, K. J. Sikes, J. Hone, H. L. Stormer, and P. Kim, *Phys. Rev. Lett.* **101**, 096802 (2008).
- [47] Y. M. Zuev, W. Chang, and P. Kim, *Phys. Rev. Lett.* **102**, 096807 (2009).
- [48] S. Das Sarma, E. H. Hwang, and E. Rossi, *Phys. Rev. B* **81**, 161407(R) (2010).
- [49] S. Das Sarma and E. H. Hwang, *Phys. Rev. Lett.* **83**, 164 (1999).
- [50] A. Iurov, G. Gumbs, D. H. Huang, and G. Balakrishnan, *Phys. Rev. B* **96**, 245403 (2017).
- [51] D. H. Huang, C. Rhodes, P. M. Alsing, and D. A. Cardimona, *J. Appl. Phys.* **100**, 113711 (2006).
- [52] D. H. Huang, G. Gumbs, and O. Roslyak, *Phys. Rev. B* **83**, 115405 (2011).
- [53] V. Y. Tsaran, A. Kavokin, S. Sharapov, A. Varlamov, and V. Gusynin, *Sci. Rep.* **7**, 10271 (2017).
- [54] A. Iurov, G. Gumbs, and D. H. Huang, *J. Phys.: Condens. Matter* **29**, 135602 (2017).
- [55] E. V. Gorbar, V. P. Gusynin, V. A. Miransky, and I. A. Shovkovy, *Phys. Rev. B* **66**, 045108 (2002).
- [56] E. H. Hwang and S. Das Sarma, *Phys. Rev. B* **79**, 165404 (2009).
- [57] S. Das Sarma and Q. Li, *Phys. Rev. B* **87**, 235418 (2013).
- [58] B. Wunsch, T. Stauber, F. Sols, and F. Guinea, *New J. Phys.* **8**, 318 (2006).
- [59] P. Pyatkovskiy, *J. Phys.: Condens. Matter* **21**, 025506 (2008).
- [60] B. Van Duppen, P. Vasilopoulos, and F. M. Peeters, *Phys. Rev. B* **90**, 035142 (2014).
- [61] P. F. Maldague, *Surf. Sci.* **73**, 296 (1978).
- [62] A. Scholz, T. Stauber, and J. Schliemann, *Phys. Rev. B* **88**, 035135 (2013).
- [63] L. A. Falkovsky, *J. Phys.: Conf. Ser.* **129**, 012004 (2008).
- [64] L. A. Falkovsky, *Phys. Usp.* **51**, 887 (2008).
- [65] L. A. Falkovsky and S. S. Pershoguba, *Phys. Rev. B* **76**, 153410 (2007).

- [66] K. F. Mak, M. Y. Sfeir, Y. Wu, C. H. Lui, J. A. Misewich, and T. F. Heinz, *Phys. Rev. Lett.* **101**, 196405 (2008).
- [67] A. Iurov, D. H. Huang, G. Gumbs, W. Pan, and A. A. Maradudin, *Phys. Rev. B* **96**, 081408 (2017).
- [68] V. P. Gusynin and S. G. Sharapov, *Phys. Rev. B* **73**, 245411 (2006).
- [69] A. Singh, K. I. Bolotin, S. Ghosh, and A. Agarwal, *Phys. Rev. B* **95**, 155421 (2017).
- [70] J. P. Carbotte, J. P. F. LeBlanc, and E. J. Nicol, *Phys. Rev. B* **85**, 201411 (2012).
- [71] A. Scholz and J. Schliemann, *Phys. Rev. B* **83**, 235409 (2011).
- [72] A. Iurov, G. Gumbs, D. Huang, and V. M. Silkin, *Phys. Rev. B* **93**, 035404 (2016).
- [73] T. Stauber, N. M. R. Peres, and A. K. Geim, *Phys. Rev. B* **78**, 085432 (2008).
- [74] Z. M. Ziman, *Principles of the Theory of Solids* (Press Syndicate of the University of Cambridge, Cambridge, 1972).
- [75] E. H. Hwang and S. Das Sarma, *Phys. Rev. B* **77**, 195412 (2008).
- [76] T. Ando, *J. Phys. Soc. Jpn.* **75**, 074716 (2006).
- [77] O. Kibis, *Phys. Rev. B* **81**, 165433 (2010).
- [78] K. Kristinsson, O. Kibis, S. Morina, and I. Shelykh, *Sci. Rep.* **6**, 20082 (2016).